Submitted to the 30th International Conference on High-Energy Physics ICHEP2000,
Osaka, Japan, July 2000

Measurement of Neutral and Charged Current Cross Sections in Electron-Proton Collisions at High Q^2 at HERA

H1 Collaboration

Abstract

The inclusive $e^- p$ single and double differential cross sections for neutral and charged current processes are measured with the H1 detector at HERA. The cross sections are measured in the range of four-momentum transfer squared Q^2 between 200 and $30\,000$ GeV^2, and Bjorken x between 0.0032 and 0.65. The data were taken with the H1 detector at HERA in 1998 and 1999 with a centre-of-mass energy of 320 GeV, and correspond to an integrated luminosity of $15.3\ \mathrm{pb}^{-1}$. The data are compared with recent measurements of the inclusive neutral and charged current $e^+ p$ cross sections. Clear evidence is observed for neutral current parity violating Z^0 exchange and the structure function $\tilde{F}_3$ is extracted. The data are found to be in good agreement with Standard Model predictions.

Abstract: 971
Parallel session: 11
Plenary talk: 7 b

1 Introduction

Inclusive Deep Inelastic Scattering (DIS) cross sections have long been used as sensitive probes of proton structure and QCD dynamics. Since 1992 the experiments H1 and ZEUS have used the colliding lepton–proton beams of the HERA accelerator to further extend the phase space of such measurements into new kinematic regions of large four-momentum transfer squared, Q^2, and small x, where x is the Bjorken scaling variable. The large integrated luminosity collected by the experiments has allowed measurements to be made in the very high Q^2 range up to $30\,000$ GeV^2. In this region where $Q^2 \simeq M_Z^2$ or M_W^2, the Z^0 and $W^\pm$ boson masses squared, the effects of the electroweak sector of the Standard Model can be tested in DIS. In addition signals of new physics beyond the Standard Model may be expected to arise at the highest Q^2 where the smallest distance scales of proton structure are probed.

Both contributions to DIS, neutral current (NC) interactions, $ep \to eX$, and charged current (CC) interactions, $ep \to \nu X$ can be measured at HERA and give complementary information on the QCD and electroweak parts of the Standard Model. The cross sections are defined in terms of two of the kinematic variables Q^2, x, and y, where y quantifies the inelasticity of the interaction.

Preliminary measurements of the Q^2 dependence of the NC and CC cross sections from e^-p scattering have already been presented[1]. These results were based on an integrated luminosity of $5.2\ \mathrm{pb}^{-1}$. In this paper we report on the NC and CC cross section measurements using the full e^-p integrated luminosity taken during the 1998/1999 running period. The data sample consists of $15.3\ \mathrm{pb}^{-1}$ obtained when HERA operated with electron beams at 27.6 GeV colliding with proton beams at an increased energy of 920 GeV, compared with 820 GeV in previous years, yielding a centre-of-mass energy $\sqrt{s} \approx 320$ GeV. The data are compared with NC and CC measurements [2] from H1 of e^+p scattering taken at a centre-of-mass energy $\sqrt{s} \approx 300$ GeV. Recently measurements of the NC and CC cross sections at high Q^2 have been reported by the ZEUS experiment [3].

2 Neutral and Charged Current Cross Sections

The NC cross section for the process $e^\pm p \to e^\pm X$ with unpolarized beams is given by

$$\frac{\mathrm{d}^2\sigma^\pm_{NC}}{\mathrm{d}x\ \mathrm{d}Q^2} = \frac{2\pi\alpha^2}{xQ^4}\left[Y_+\tilde{F}_2 \mp Y_-x\tilde{F}_3 - y^2\tilde{F}_{_L}\right] \quad , \tag{1}$$

where α is the fine structure constant taken to be $\alpha \equiv \alpha(Q^2 = 0)$ and the helicity dependences of the electroweak interactions are contained in the functions $Y_\pm \equiv 1 \pm (1-y)^2$. The dominant contribution to the cross section comes from the structure function $\tilde{F}_2$. The $\tilde{F}_{_L}$ contribution is largest at high y and is expected to diminish with increasing Q^2, whereas the structure function $x\tilde{F}_3$ contributes in the high Q^2 regime of Z^0 exchange. Note that for unpolarized beams, $\tilde{F}_2$ is the same for electron and for positron scattering, while the $x\tilde{F}_3$ contribution changes sign as can be seen in eq. 1.

It is convenient to derive from the measured $\mathrm{d}^2\sigma/\mathrm{d}x\mathrm{d}Q^2$ the NC "reduced cross section" in which part of the Q^2 dependence of $\mathrm{d}^2\sigma/\mathrm{d}x\mathrm{d}Q^2$ due to the photon propagator is removed

$$\tilde{\sigma}_{NC}(x,Q^2) \equiv \frac{1}{Y_+}\,\frac{Q^4\,x}{2\pi\alpha^2}\,\frac{\mathrm{d}^2\sigma_{NC}}{\mathrm{d}x\mathrm{d}Q^2} \quad . \tag{2}$$

The leading order double differential CC cross section for $e^- p \to \nu X$ can be written as

$$\frac{\mathrm{d}^2\sigma_{CC}}{\mathrm{d}x\;\mathrm{d}Q^2} = \frac{G_F^2}{2\pi x}\left(\frac{M_W^2}{M_W^2+Q^2}\right)^2 x\left[(u+c)+(1-y)^2(\bar{d}+\bar{s})\right] \quad , \tag{3}$$

where G_F is the Fermi coupling constant, and u, c, $\bar{d}$, $\bar{s}$ are the quark distributions. The description of $e^+ p \to \bar{\nu} X$ is obtained by changing all quarks with anti-quarks (and vice-versa) in eq. 3. The CC reduced cross section is defined as

$$\tilde{\sigma}_{CC}\,(x,Q^2) \equiv \frac{2\pi\,x}{G_F^2}\left(\frac{M_W^2+Q^2}{M_W^2}\right)^2 \frac{\mathrm{d}^2\sigma_{CC}}{\mathrm{d}x\mathrm{d}Q^2} \quad . \tag{4}$$

3 Experimental Technique

3.1 Detector and Kinematic Reconstruction

The H1 detector is described in detail elsewhere [4]. The co-ordinate system of H1 defines the positive z axis to be in the direction of the incident proton beam. The polar angle θ is then defined with respect to the positive z axis. The forward direction is the region of increasing z.

In order to determine acceptance corrections and background contributions for the DIS cross section measurements, the detector response to events produced by various Monte Carlo generation programs is simulated in detail, and is described in [2].

The present analysis closely follows that of ref. [2], and is briefly described below. The NC event kinematics are reconstructed using the energy and polar angle of the scattered electron, E'_e and θ_e respectively. The total $E-p_z$ of the event is then obtained from the relation $E-p_z = \Sigma + E'_e(1-\cos\theta_e)$. Here $\Sigma = \sum_i (E_i - p_{z,i})$, where the summation is performed over all hadronic final state particles. These quantities are used to determine the kinematic variables x, Q^2 , and y in the $e\Sigma$ method [5]:

$$y_{e\Sigma} = 2E_e\frac{\Sigma}{(E-p_z)^2} \qquad Q^2_{e\Sigma} = \frac{P^2_{T,e}}{1-y_e} \qquad x_{e\Sigma} = \frac{P^2_{T,e}}{s\;y_\Sigma(1-y_\Sigma)} \quad , \tag{5}$$

where E_e is the incident electron beam energy, and

$$y_\Sigma = \frac{\Sigma}{E-p_z} \qquad y_e = 1-\frac{E'_e(1-\cos\theta_e)}{2\;E_e} \qquad P_{T,e} = E'_e\sin\theta_e \quad . \tag{6}$$

The resolution of the reconstruction method is controlled by requiring the purity and stability of any (x, Q^2) bin to be larger than 30%. The stability (purity) is defined as the fraction of

events which originate from a bin and which are reconstructed in it, divided by the number of generated (reconstructed) events in that bin.

The CC event kinematics can only be determined with the hadron method (h method) [6]. The h method kinematic variables are reconstructed using the relations

$$y_h = \frac{\Sigma}{2\ E_e} \qquad Q^2_h = \frac{P^2_{T,h}}{1-y_h} \qquad x_h = \frac{Q^2_h}{s\ y_h} \quad , \tag{7}$$

where $P_{T,h} = \sqrt{(\sum_i p_{x,i})^2 + (\sum_i p_{y,i})^2}$ and is summed over all particles of the hadronic final state. This method is influenced by particle losses in the beam pipe and fluctuations of the detector response to hadronic final state particles, and therefore has moderate precision.

3.2 Measurement Procedure

The electromagnetic and hadronic response of the detector is calibrated using the analysis described in [2]. The procedure is found to give good agreement between data and simulation. The systematic uncertainty of the absolute electromagnetic energy scale varies from 1% in the backward region to 3% in the forward region of the calorimeter. For the hadronic energy scale a conservative uncertainty of 3% is assigned.

High Q^2 NC events are selected by requiring that the event has a compact electromagnetic cluster, taken to be the scattered electron, in addition to a vertex position within ± 35 cm of its nominal position. The cluster is validated by requiring that an extrapolated track have a distance of closest approach to the cluster of less than 12 cm. This is only applied for $\theta_e \geq 40^\circ$, where θ_e is the polar angle of the scattered electron. In this analysis the polar angle is determined using the position of the electromagnetic cluster and assigned a systematic uncertainty of 3 mrad. The energy of the cluster, E'_e, is required to be larger than 11 GeV where the trigger is very efficient. The total $E - P_z$ summed over all particles is required to be larger than 35 GeV to reduce the photo-production background, and the influence of QED radiative corrections to the measured cross sections. Fiducial cuts are also made to remove local regions where the electromagnetic shower of the scattered electron is not fully contained in the calorimeter, and where the trigger is not fully efficient. Since the signal to background ratio is reduced in the region of high y, a further kinematic cut is made requiring $y_e \leq 0.9$. The remaining photo-production contribution to the NC cross sections is never more than 5% at the highest y and negligible elsewhere. The double differential NC reduced cross section data have a statistical precision of $\approx 4\%$ at low Q^2 compared with a total systematic uncertainty of $\approx 7\%$ rising to 15% at high x. The total uncertainty is dominated by the statistical error for $Q^2 > 1\,000$ GeV^2. The final sample of selected data consists of about $40\,000$ events. The comparison of the data and the simulation is shown in fig.1 for the scattered electron energy spectrum, and the polar angle θ_e. Both distributions are well described by the simulation.

The selection of CC events is based on the expectation that such events have a large missing transverse momentum, $P_{T,h}$, assumed to be carried by an unseen neutrino. Therefore a requirement that $P_{T,h} \geq 12$ GeV is made. In addition the event must have a reconstructed vertex within ± 35 cm of its nominal position. The non-ep and ep background is rejected using the same method as detailed in [2]. The remaining ep background is dominantly due to

photo-production events and is negligible for most of the measured kinematic domain, though it may reach up to 3% at $Q^2 = 500\,\mathrm{GeV}^2$. The contribution is subtracted statistically from the CC data sample with a systematic uncertainty of 30% of the subtracted events. In order to restrict the measurement to a region where the kinematic reconstruction is optimal the events are required to have $y_h < 0.85$. The CC trigger efficiency is determined using NC events in which all information associated to the scattered electron is suppressed. This method gives a precise measure of the efficiency which is found to be 78% at $Q^2 = 500\,\mathrm{GeV}^2$ and reaches 99% at $Q^2 = 5000\,\mathrm{GeV}^2$. The measurement is restricted to the region where the trigger efficiency is acceptable by demanding $y_h > 0.03$. The systematic uncertainty assigned to the CC trigger efficiency varies from 2% at low $Q^2 = 500$ GeV^2 to 1% at high Q^2. Of the systematic sources of uncertainty studied the most significant contribution to the measured CC cross sections comes from the 3% uncertainty on the hadronic energy scale. This results in an uncertainty of 4% at low Q^2 and 15% at high Q^2 compared with a total systematic error of 6.5% at low Q^2 , and 16% at high Q^2 . This is comparable to the statistical precision which varies from 11% to 19% over the same Q^2 range. After all selection criteria are applied, the final CC data sample contains about 700 events. The data and simulation are compared in fig.2 for the $P_{T,h}$ and y_h spectra. In both cases the simulation gives a good description of the data.

The selected events are corrected for detector acceptance, and migrations using the simulation and converted to bin centered cross sections using the prediction from the H1 e^+p QCD fit [2]. The cross sections are corrected for the effects of QED radiation.

4 Results

The single differential cross sections $\mathrm{d}\sigma/\mathrm{dQ}^2$ for NC and CC e^-p data are shown in fig.3 for $y \leq 0.9$. [1] The data are compared with the H1 e^+p measurements and the NLO QCD fit performed on low Q^2 fixed target data from NMC and BCDMS and H1 e^+p data called "H1 e^+p QCD fit" in the following. The new e^-p NC and CC measurements presented here were not included in the QCD fit. The lower figures show the ratio of the preliminary measurements to the Standard Model expectation. The global 3% luminosity uncertainty of the new data is not included in the error bars. The Standard Model uncertainty represents the uncertainty of the expectation due to assumptions made in the H1 e^+p QCD fit, as well as the uncertainties of the experimental data entering the fit, and is detailed in [2].

The data are found to be in good agreement with the expectation. For $Q^2 > 3\,000$ GeV^2 the NC e^-p cross section is observed to be systematically larger than the e^+p cross section. The influence of the increased centre-of-mass energy is indicated by the dashed line and predicts an increased cross section of $\approx 7\%$ for $Q^2 < 1\,000$ GeV^2 rising to 50% at $Q^2 = 30\,000$ GeV^2. However, at high Q^2 this is approximately an order of magnitude smaller than the increase expected from the different lepton polarity. The cross sections are consistent with the Standard Model expectation of the parity violating contribution of Z^0 exchange.

The CC cross section Q^2 dependence is shown in fig.3b and compared with the e^+p measurements. The e^-p data are found to have a larger cross section everywhere, by up to a factor

[1] These measured NC cross sections are corrected for the small effect of the cut $E'_e > 11$ GeV. Similarly the CC cross sections are corrected for the cuts $0.03 < y < 0.85$

of ten at $Q^2 = 15\,000\text{GeV}^2$. The effect of the increased centre-of-mass energy is expected to be relatively small, and is shown as the dashed curve in fig.3b. The CC electron scattering cross section is in good agreement with the Standard Model expectation based on the H1 e^+p QCD fit. The ratio of data to expectation is shown in fig.3d together with the Standard Model Uncertainty.

The integrated x dependence of the NC cross sections are shown in fig.4 for both e^-p and e^+p scattering. The data are shown for $Q^2 > 1\,000$ GeV^2 and $y < 0.9$ in fig.4a,b and are in agreement with the expectation from the Standard Model. The larger centre-of-mass energy for the e^-p scattering data yields a larger cross section by $\simeq 25\%$ at low x. The cross sections are also measured for $Q^2 > 10\,000$ GeV^2, $y < 0.9$ (fig.4c,d) and are approximately a factor of four larger than for e^+p scattering at $x \simeq 0.2$ of which 12% is due to the different centre-of-mass energies. The dashed curves show the Standard Model expectation under the assumption of pure photon exchange. For electron scattering the Z^0 exchange contribution enhances the cross section, whilst in e^+p scattering it reduces the cross section.

The integrated CC cross section $\mathrm{d}\sigma/\mathrm{d}x$ is measured for $Q^2 > 1\,000$ GeV^2, and $y < 0.9$ and is shown in fig.5 compared with the same measurement in e^+p scattering. The new data are found to be in good agreement with the expectation. The cross sections are larger than for positron scattering by a factor of two at low x and a factor of four at high x. The influence of the centre-of-mass energy accounts for a small part of the increased cross section, the remainder being due to the different quarks which couple to the $W^\pm$ in $e^\pm p$ scattering.

The double differential NC reduced cross section is shown in fig.6 over the full x and Q^2 range of the measurement which reaches $x = 0.65$ and $Q^2 = 30\,000$ GeV^2. The data are compared with the H1 e^+p QCD fit, and are found to give a good prediction of the x, Q^2 behaviour of the data. In fig.7 the data at high x are compared with the measurements of e^+p scattering as a function of Q^2. They are compared with the cross sections determined from the H1 e^+p QCD fit. The data are found to be in agreement with the e^+p measurements for $Q^2 < 2\,000$ GeV^2.

At large Q^2, and at lower x, the two data-sets differ as expected from $x\tilde{F}_3$contributions to the NC cross sections. This structure function is extracted using the equation

$$\tilde{\sigma}^-_{NC} - \tilde{\sigma}^+_{NC} \;=\; x\tilde{F}_3 \left[\frac{Y_{-\,920}}{Y_{+\,920}} + \frac{Y_{-\,820}}{Y_{+\,820}}\right] - \tilde{F}_{_L} \left[\frac{y^2_{920}}{Y_{+\,920}} + \frac{y^2_{820}}{Y_{+\,820}}\right] \quad , \tag{8}$$

where the functions $Y_{\pm\,920}$ and $Y_{\pm\,820}$ are the usual electroweak helicity functions evaluated for the given proton beam energy. Since the cross section measurements are made for fixed x and Q^2, any change in centre-of-mass energy translates into a change in y and hence affects the helicity functions. For the determination of $x\tilde{F}_3$ the small contribution of $\tilde{F}_{_L}$ is taken from the QCD fit. In order to optimise the sensitivity to $x\tilde{F}_3$, both the e^+p and the e^-p reduced cross sections are rebinned into two Q^2 bins with centres $Q^2 = 2\,500$ GeV^2 and $Q^2 = 10\,000$ GeV^2. The reduced cross sections and the resulting measurement of $x\tilde{F}_3$ are shown in fig.8 compared with the H1 e^+p QCD fit. The systematic errors for each reduced cross section are evaluated for these bins. The data are in good agreement with the expectation. The data are observed to peak at $x \simeq 0.1$ reflecting the valence structure of the constituent quarks.

The double differential CC reduced cross section is shown in fig.9 compared with the measurements from e^+p scattering. The data are well described by the H1 e^+p QCD fit. The cross sections measured in e^-p scattering are found to be consistently larger than for e^+p scattering everywhere. The difference in the cross sections is found to increase with Q^2. This is expected within the Standard Model and is due to the different quark densities probed in e^+p and e^-p scattering.

5 Summary

The NC and CC cross sections have been measured for e^-p scattering at a centre-of-mass energy of $\sqrt{s} \approx 320$ GeV. Standard Model expectations based on the H1 e^+p QCD fit to NMC, BCDMS, and H1 e^+p data [2] are able to provide a good description of all the measured cross sections.

Comparisons of these cross sections with the H1 measurements of NC and CC cross sections in e^+p scattering are made. The NC e^-p measurement of $\mathrm{d}\sigma/\mathrm{d}Q^2$ shows a clear increase with respect to the positron scattering cross sections at high Q^2, consistent with the expectation of the contribution of Z^0 exchange. The CC cross section is observed to be larger for electron scattering than for positron scattering by up to a factor of ten at high Q^2 . The influence of larger centre-of-mass energy is responsible for only a small part of the cross section increase. The NC and CC cross sections $\mathrm{d}\sigma/\mathrm{d}x$ are presented for $Q^2 > 1\,000$ GeV^2 and $y < 0.9$. In addition the NC cross section is also measured for $Q^2 > 10\,000$ GeV^2 and found at low x to be approximately a factor of four larger than for e^+p scattering.

The double differential NC reduced cross sections are measured in the Q^2 range $200 \leq Q^2 \leq 30\,000$ GeV^2, and $0.0032 \leq x \leq 0.65$. The data agree well with measurements for e^+p scattering for $Q^2 < 2\,000$ GeV^2. At higher Q^2 the expected enhancement of the cross section due to Z^0 exchange is observed and the structure function $x\tilde{F}_3$ is measured in the range $0.032 < x < 0.65$ and $2\,500 \leq Q^2 \leq 10\,000$ GeV^2. The double differential CC reduced cross section is presented for the range $500 \leq Q^2 \leq 15\,000$ GeV^2, and $0.013 \leq x \leq 0.4$. The data are found to be larger than for positron scattering as predicted by the Standard Model.

Acknowledgments

We are grateful to the HERA machine group whose outstanding efforts have made and continue to make this experiment possible. We thank the engineers and technicians for their work in constructing and now maintaining the H1 detector, our funding agencies for financial support, the DESY technical staff for continual assistance, and the DESY directorate for the hospitality which they extend to the non-DESY members of the collaboration.

References

[1] V. Chekelian, Rencontres de Moriond on Electroweak Interactions and Unified Theories, March 1999, Les Arcs, France.

[2] H1 Collab., 'Measurement of Neutral and Charged Current Cross Sections in Positron-Proton Collisions at Large Momentum Transfer at HERA', paper 157ai contributed to International Europhysics Conference on High Energy Physics, 15-21 July 1999, Tampere, Finland HEP99

[3] ZEUS Collab., J.Breitweg et al. , DESY 99-056 (1999), *accepted by Eur. Phys. J.*
ZEUS Collab., J.Breitweg et al. , DESY 99-057 (1999), *submitted to Eur. Phys. J.*

[4] H1 Collab., I. Abt et al., *Nucl. Instrum. Methods* **A 386** (1997) 310 and 348.

[5] U. Bassler and G. Bernardi, Nucl. Instr. Meth. **A361** (1995) 197;
U. Bassler and G. Bernardi, Nucl. Instr. Meth. **A426** (1999) 583.

[6] A. Blondel and F. Jacquet, Proceedings of the Study of an ep Facility for Europe, ed. U. Amaldi, DESY 79/48 (1979) 391.

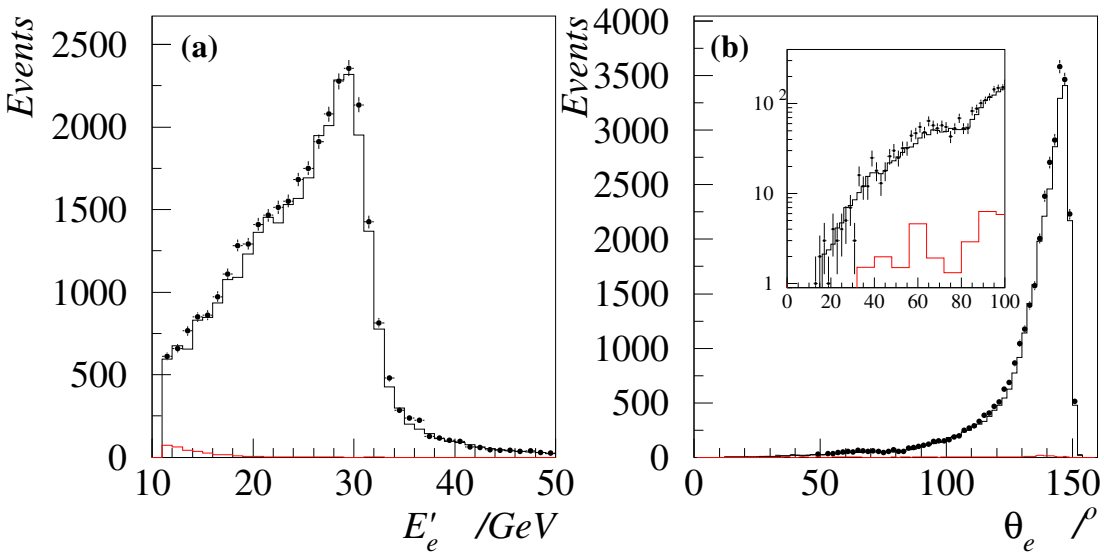

Figure 1: Distributions of (a) E'_e and (b) θ_e for NC data (solid points) and simulation (solid line). The lower histograms show the photo-production contribution. The inset in (b) shows an enlargement of the low θ_e distribution.

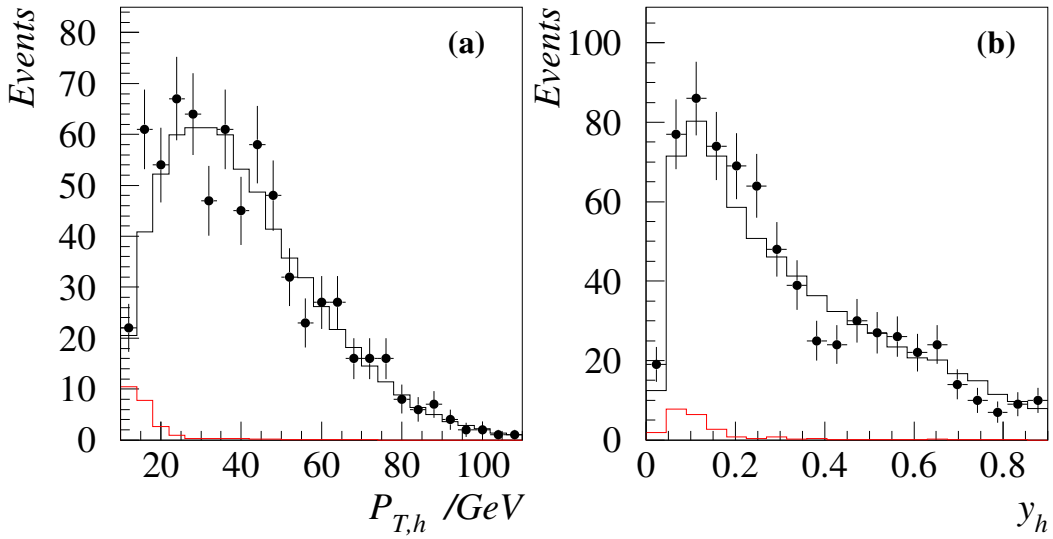

Figure 2: Distributions of (a) $P_{T,h}$ and (b) y_h for CC data (solid points) and simulation (solid line). The lower histograms show the photo-production contribution.

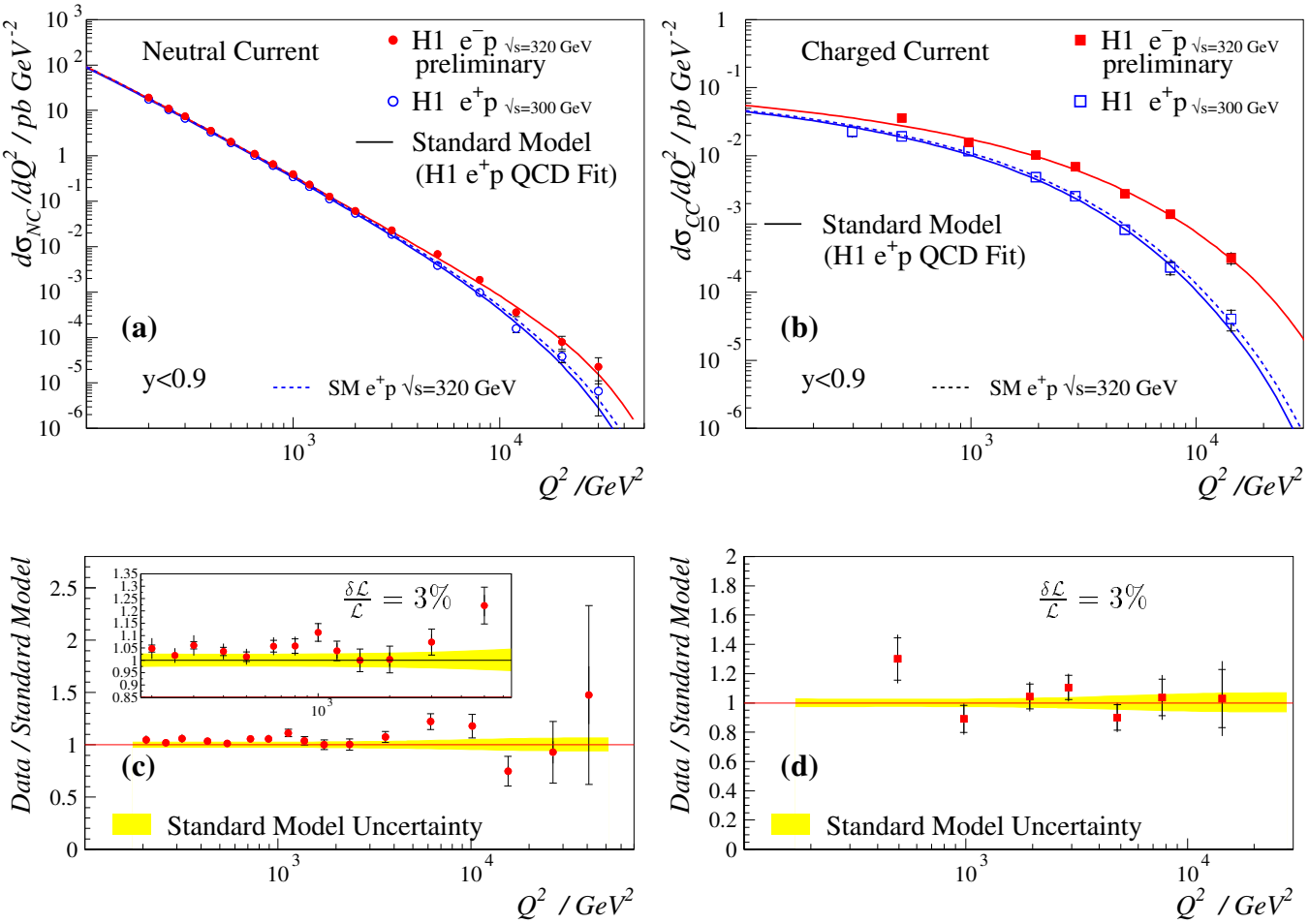

Figure 3: The Q^2 dependence of the NC (a) and CC (b) cross sections $d\sigma/dQ^2$ are shown for the preliminary e^-p (solid points) and e^+p (open points) measurements. The data are compared with the Standard Model expectation determined from the H1 e^+p QCD fit including the H1 e^+p data. The influence of the increased centre-of-mass energy is shown as the dashed curve. The ratio of the e^-p data to the Standard Model expectation is shown in figures (c) and (d) for NC and CC respectively. The Standard Model Uncertainty is shown as the shaded band. The 3% luminosity uncertainy is not included in the error bars.

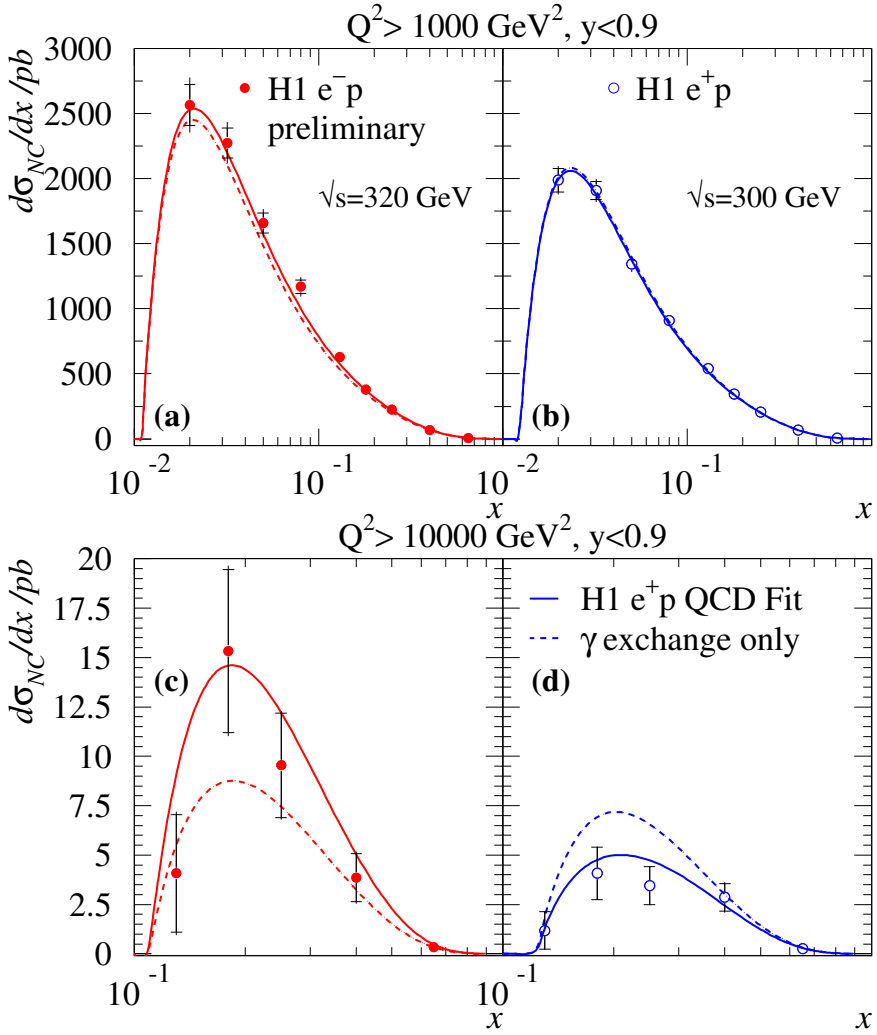

Figure 4: The NC cross sections $d\sigma/dx$ for the preliminary e^-p data are shown in (a) for $Q^2 > 1\,000$ GeV^2 and in (c) for $Q^2 > 10\,000$ GeV^2. The H1 e^+p cross sections are shown in (b) and (d) for $Q^2 > 1\,000$ GeV^2 and $10\,000$ GeV^2 respectively. The solid curves show the Standard Model expectation based on the H1 e^+p QCD fit. The dashed curves show the contribution of photon exchange only. All cross sections are shown for $y < 0.9$.

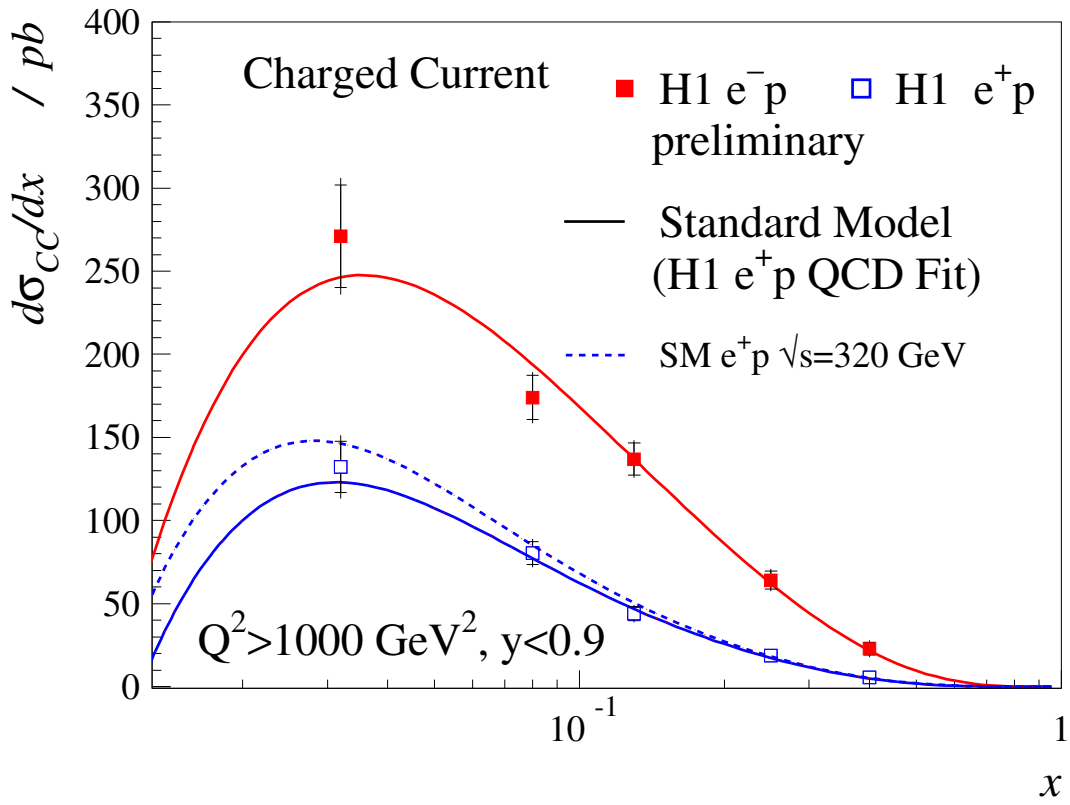

Figure 5: The CC cross section $d\sigma/dx$ for $Q^2 > 1\,000$ GeV^2 and $y < 0.9$ is shown for the preliminary H1 e^-p data (solid points) and the H1 e^+p data (open points). The solid curves show the Standard Model expectation based on the H1 e^+p QCD fit. The dashed curve shows the influence of the increased centre-of-mass energy.

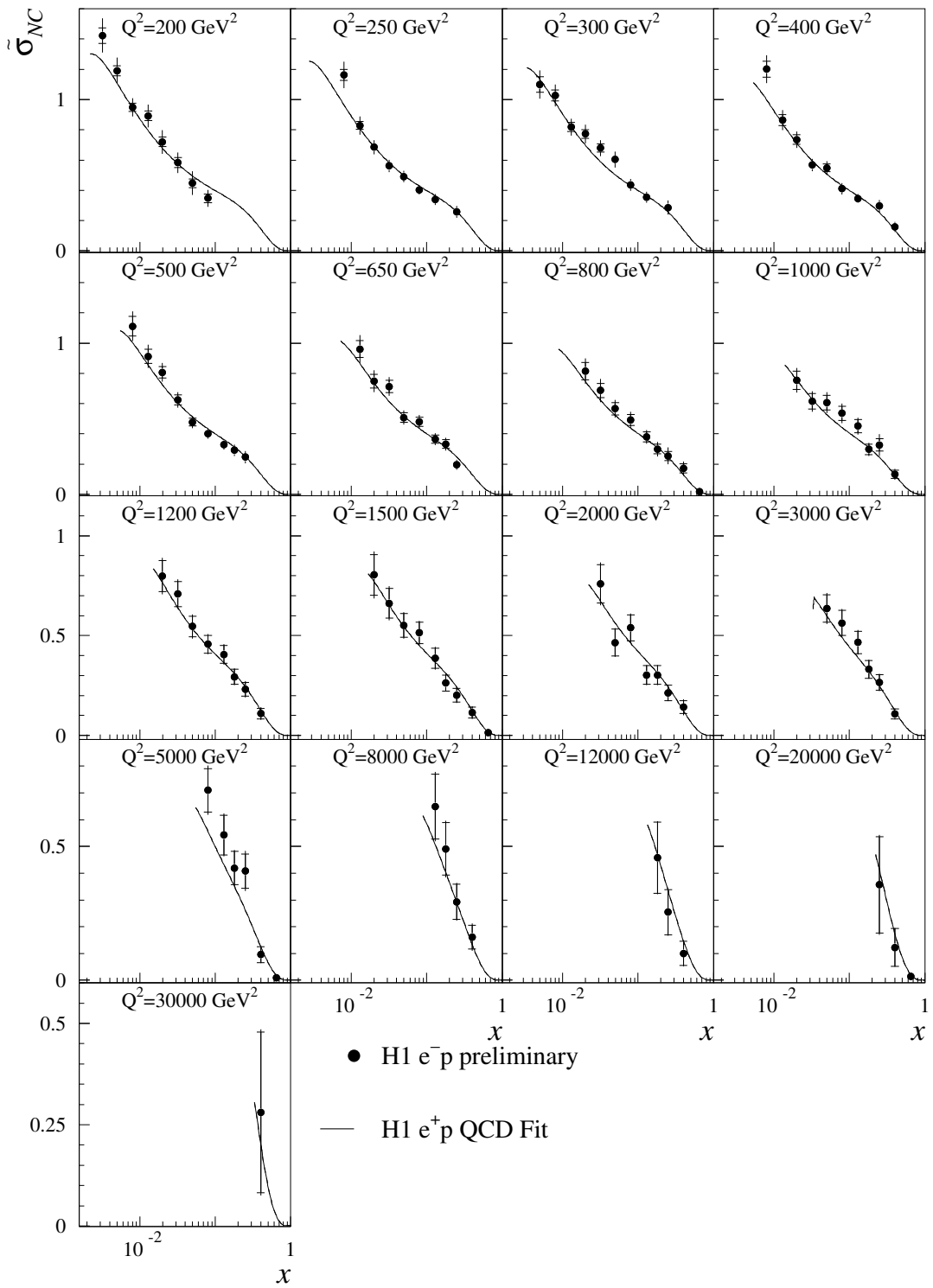

Figure 6: The NC $e^- p$ reduced cross section $\tilde{\sigma}_{NC}(x, Q^2)$ is compared with the H1 $e^+ p$ QCD fit. The inner error bars represent the statistical error, and the outer error bars show the total error.

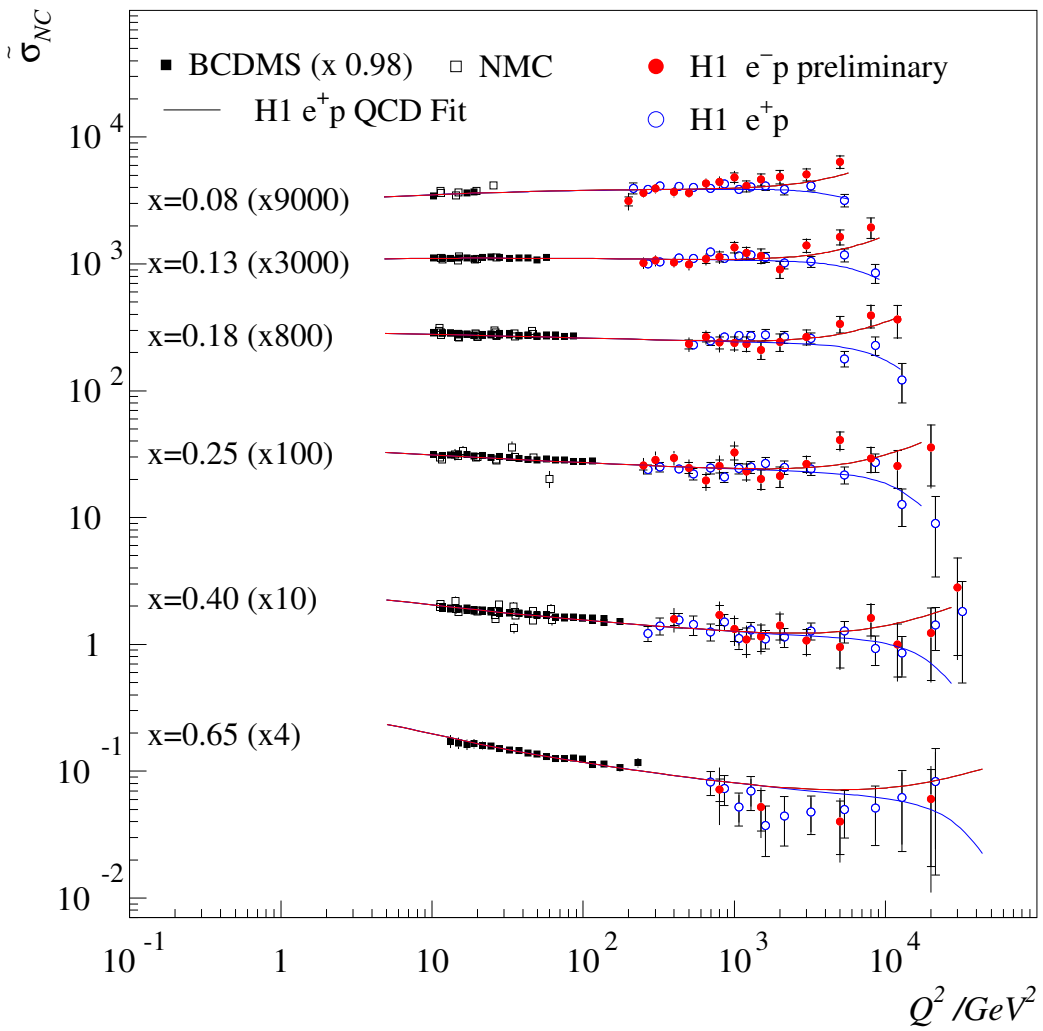

Figure 7: The NC reduced cross section $\tilde{\sigma}_{NC}(x, Q^2)$ is shown at high x compared with the H1 e^+p QCD fit. The preliminary e^-p data with $\sqrt{s} \approx 320$ GeV (solid points) are compared with the H1 e^+p data at $\sqrt{s} \approx 300$ GeV (open points). The solid curves represent the Standard Model expectation based on the H1 e^+p QCD fit. The inner error bars represent the statistical error, and the outer error bars show the total error.

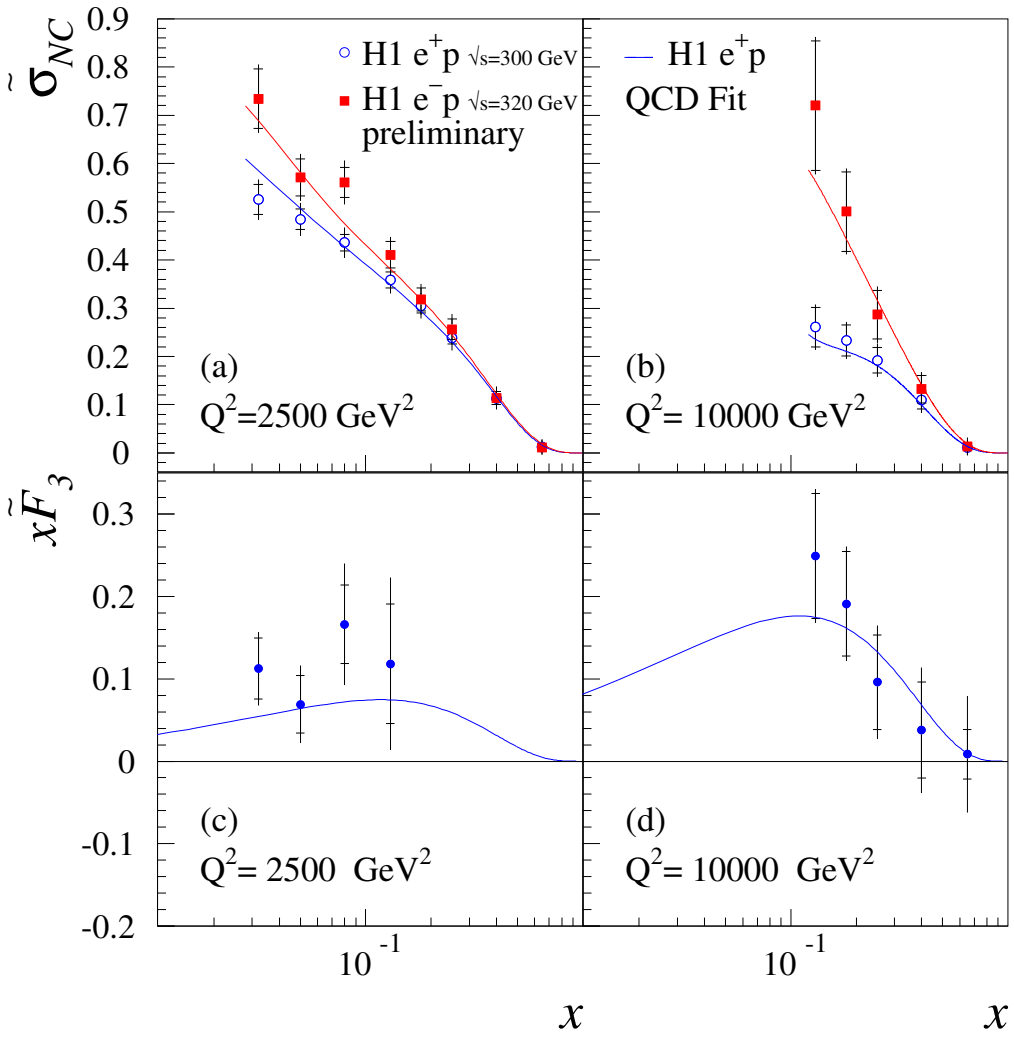

Figure 8: The NC reduced cross section $\tilde{\sigma}_{NC}(x, Q^2)$ is shown compared with the H1 e^+p QCD fit at (a) $Q^2 = 2\,500$ GeV^2 and (b) $Q^2 = 10\,000$ GeV^2. The preliminary e^-p data with $\sqrt{s} \approx 320$ GeV (solid points) are compared with the H1 e^+p data at $\sqrt{s} \approx 300$ GeV (open points). The solid curves represent the Standard Model expectation based on the H1 e^+p QCD fit. The parity violating structure function $x\tilde{F}_3$ is compared with the H1 e^+p QCD fit at (c) $Q^2 = 2\,500$ GeV^2 and (d) $Q^2 = 10\,000$ GeV^2. In all figures the inner error bars represent the statistical error, and the outer error bars show the total error.

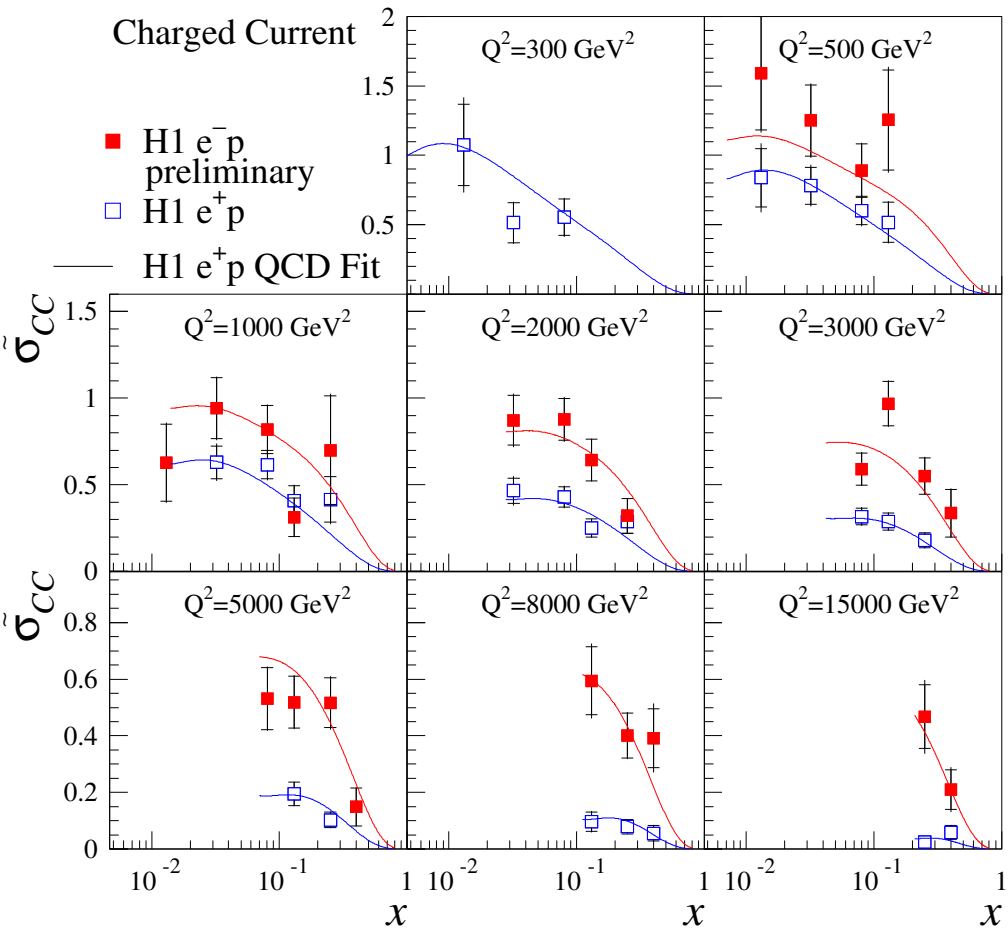

Figure 9: The CC reduced cross section $\tilde{\sigma}_{CC}(x, Q^2)$ is shown for e^-p scattering at $\sqrt{s} \approx 300$ GeV (solid squares) and e^+p scattering at with $\sqrt{s} \approx 320$ GeV (open squares). The data are compared with the H1 e^+p QCD fit. The inner error bars represent the statistical error, and the outer error bars show the total error.